Brief Report

Sun Kyoung Kim*

Correlations for friction factor of Carreau fluids in a laminar tube flow

https://doi.org/10.1515/arh-2025-0033
received October 14, 2024; accepted February 08, 2025

Abstract: This study presents an improved approach to correlating the Darcy friction factor for a fully developed laminar flow of Carreau fluids in circular pipes. The Carreau model stands as an essential representation of viscosity behavior and captures the complex rheological characteristics of polymeric fluids. By deriving a semi-analytical form of the Darcy friction factor, the study enables rapid and repeated evaluations across diverse flow conditions, facilitating the development of an explicit correlation. This improved correlation, built upon extensive data analysis, offers enhanced accuracy and broader applicability in predicting fluid behavior. The practical significance of this advancement is demonstrated through its successful application in calculating pressure drops for polymer melt and blood flows, highlighting its potential impact on industries ranging from materials processing to biomedical engineering. This work not only contributes to the theoretical understanding of non-Newtonian fluid dynamics but also provides a valuable tool for engineers dealing with complex fluid systems in circular pipes.

Keywords: Darcy friction factor, Carreau fluid, laminar flow, circular tube, correlation

Nomenclature

f	Darcy friction factor
f_N	Darcy friction factor for a Newtonian fluid
$f\mathrm{Re}$	Poiseuille number
G	intermediate function I_1 in the Carreau model
I_1	WRM integral
K_1	approximated consistency
n	index in the viscosity model
n_1	apparent index
n_2	modified apparent index
p	pressure
Q	flow rate
q	core flow rate
R	radius
r	radial position
Re	Reynolds number
S	normalized shear rate ratio
S_1	normalized shear rate ratio using ϕ_1
S_2	normalized shear rate ratio using ϕ_2
u	velocity along x
u_m	mean velocity
x	axial position
Γ	dimensionless apparent shear rate ($=\lambda\dot{\gamma}_a$)
$\dot{\gamma}$	shear rate
$\dot{\gamma}_a$	apparent shear rate
$\dot{\gamma}_w$	wall shear rate
ϕ	shear rate ratio
ϕ_p	shear rate ratio of power law $\left(=\frac{3n+1}{4n}\right)$
ϕ_1	approximate shear rate ratio using n_1 ($=\phi_p(n_1)$)
ϕ_2	approximate shear rate ratio using n_2 ($=\phi_p(n_2)$)
η	viscosity
η_0	zero-shear viscosity
η_a	apparent viscosity (viscosity at $\dot{\gamma}_a$)
η_p	power law viscosity
η_∞	infinite-shear viscosity
φ	dimensionless truncation viscosity $\left(=\frac{\eta_\infty}{\eta_0}\right)$
λ	time constant
ρ	density
τ	shear stress
τ_w	wall shear stress
ψ	viscosity ratio $\left(=\frac{\eta_w}{\eta_a}\right)$
ψ_c	viscosity ratio for the Carreau model
ψ_p	viscosity ratio for the power law model ($=\phi_p^{n-1}$)

1 Introduction

Laminar flow through circular tubes is a critical aspect of fluid engineering, especially in processes involving generalized

* **Corresponding author: Sun Kyoung Kim**, Department of Mechanical System Design Engineering, Seoul National University of Science and Technology, Seoul, 01811, Republic of Korea, e-mail: sunkkim@seoultech.ac.kr

Newtonian fluids (GNFs). Accurate evaluation of pressure drops is essential for the precise design of flow systems. The power law model, while effective in approximating shear thinning behavior at high shear rates, has notable limitations at low shear rates. Despite these limitations, its simplicity has facilitated extensive analytical developments and remains a cornerstone tool for designing flow systems of GNF fluids [1–3].

Recent advancements in simulation tools have significantly enhanced the evaluation of pressure drops in laminar flow fields, even for complex GNFs [4–6]. However, there is a growing need for more accurate friction factor analyses for various GNF models. A recent approach involves using the apparent power law index, determined from the instantaneous slope of the nonlinear constitutive relation in the log–log plane at the apparent shear rate [7]. This method, although applicable to various constitutive models, suffers from errors due to the loose connection between the true wall shear stress and the estimated wall shear stress [2,8].

This study aims to develop an enhanced correlation for the laminar, fully developed tube flow of Carreau fluids [9], building on the functional form proposed by the apparent index method. The Carreau model is a seminal representation of viscosity behavior, capturing the complex rheological characteristics of polymeric fluids with elegance [10–12]. By leveraging the Weissenberg–Rabinowitsch–Mooney (WRM) framework [13], we determine the model coefficients through a semi-analytical solution, ensuring high accuracy as long as the solutions of the involved nonlinear equations are precise [9,14].

To construct the correlation model, we introduce the shear rate ratio and viscosity ratio, along with three functions that modify the apparent index. These modifications, proven effective in previous convection analysis, are optimized through an efficient objective function [15]. The parameters of these functions are established and validated through comparison with a foundational dataset derived from the previously mentioned semi-analytical solutions. This methodology significantly lowers computational requirements compared to traditional numerical methods while also enhancing the accuracy of the solutions.

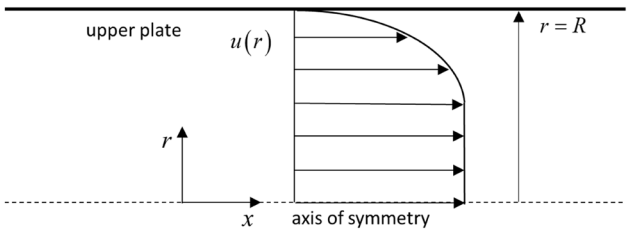

Figure 1: Schematic of the fully developed laminar flow in a circular, straight tube with radius R.

As a result, it enables the generation of accurate, exhaustive solutions across a comprehensive range of parameters. The derived correlations undergo rigorous validation against the semi-analytical solutions and existing correlations. Our enhanced correlation not only improves the precision of friction factor estimations but also exhibits remarkable adaptability and real-world applicability. This is evidenced by its successful extension to modeling both polypropylene (PP) melt flow and blood flow dynamics.

2 Formulation

2.1 Pressure gradient and shear stress

Since the pressure gradient in the flow direction x, $\partial p/\partial x$, is constant over the fully developed region shown in Figure 1, the wall shear stress is described as

$$\tau_w = \tau(R) = -\frac{R}{2}\frac{\partial p}{\partial x}. \tag{1}$$

Then, the shear stress is

$$\tau(r) = \tau_w \frac{r}{R}. \tag{2}$$

For a GNF, the shear stress is expressed as

$$\tau(\dot{\gamma}) = \eta(\dot{\gamma})\dot{\gamma}, \tag{3}$$

where η is the viscosity and $\dot{\gamma}$ is the shear rate given by

$$\dot{\gamma} = -\frac{\mathrm{d}u}{\mathrm{d}r}. \tag{4}$$

2.2 Core flow rate

Considering the flow rate through a subsection with the radius, r, the flow rate through the subsection is expressed as

$$q(r) = 2\pi\int_0^r ru(r)\mathrm{d}r = \pi\int_0^{r^2} u(r)\mathrm{d}r^2. \tag{5}$$

Let us define the above as the core flow rate at r. Integration of equation (5) by parts gives

$$q(r) = \pi\int_0^{r^2} u(r)\mathrm{d}r^2 = \pi u(r)r^2 - \pi\int_0^{u(r)} r^2\mathrm{d}u. \tag{6}$$

Replacing equation (4) in the above equation using equation (2), $q(r)$ is rewritten as

$$q(r) = \pi r^2 u(r) + I_1(r), \tag{7}$$

where the integration $I_1(r)$ is defined as [9]

$$I_1(r) = -\pi \int_0^{u(r)} r^2 \mathrm{d}u. \tag{8}$$

Using $r = \tau R/\tau_\mathrm{w}$ and $\mathrm{d}r = \mathrm{d}\tau R/\tau_\mathrm{w}$ from equation (2), along with $\mathrm{d}u = -\dot{\gamma}\mathrm{d}r = -\dot{\gamma}R/\tau_\mathrm{w} \cdot \mathrm{d}\tau$ from equation (4), we obtain the WRM equation

$$I_1(r) = \frac{\pi R^3}{\tau_w^3} \int_0^{\tau(r)} \dot{\gamma}(r)\tau^2 \mathrm{d}\tau. \tag{9}$$

Using equation (3), equation (9) can be rewritten as

$$I_1(\dot{\gamma}) = \frac{\pi R^3}{\dot{\gamma}_\mathrm{w}^3 \eta(\dot{\gamma}_\mathrm{w})^3} \int_0^{\dot{\gamma}} \dot{\gamma}^3 \eta(\dot{\gamma})^2 \frac{\mathrm{d}\tau}{\mathrm{d}\dot{\gamma}} \mathrm{d}\dot{\gamma}. \tag{10}$$

2.3 Mean velocity

At the tube wall ($r = R$), the core flow rate gives the whole flow rate, which is

$$Q \equiv q(R) = I_1(\dot{\gamma}_\mathrm{w}) = \frac{\pi R^3}{\dot{\gamma}_\mathrm{w}^3 \eta(\dot{\gamma}_\mathrm{w})^3} \int_0^{\dot{\gamma}_\mathrm{w}} \dot{\gamma}^3 \eta(\dot{\gamma})^2 \frac{\mathrm{d}\tau}{\mathrm{d}\dot{\gamma}} \mathrm{d}\dot{\gamma}. \tag{11}$$

The procedure given by equations (4)–(11) is called the aforementioned WRM analysis, and the details can be found in the study of Kim [9]. Now, the mean velocity is obtained by

$$u_\mathrm{m} = \frac{I_1(R;\tau_\mathrm{w})}{\pi R^2}. \tag{12}$$

2.4 Reynolds number

Assuming a Newtonian flow, the apparent shear rate is specified as

$$\dot{\gamma}_\mathrm{a} = \frac{4u_\mathrm{m}}{R}. \tag{13}$$

Then, the apparent viscosity is set as

$$\eta_\mathrm{a} = \eta(\dot{\gamma}_\mathrm{a}). \tag{14}$$

Then, let us define the Reynolds number as

$$\mathrm{Re} = \frac{\rho u_\mathrm{m}(2R)}{\eta_\mathrm{a}}, \tag{15}$$

where ρ is the density of the fluid.

2.5 Darcy friction factor

The Darcy friction factor can be expressed as

$$f = \frac{8\tau_\mathrm{w}}{\rho u_\mathrm{m}^2}, \tag{16}$$

which is the ratio of the wall friction force to the dynamic pressure force. Note that it is four times the Fanning friction factor. Then, the substitution of equations (14) and (15) into equation (16) gives

$$f = \frac{64}{\mathrm{Re}} \frac{\dot{\gamma}_\mathrm{w}\eta_\mathrm{w}}{\dot{\gamma}_\mathrm{a}\eta_\mathrm{a}}. \tag{17}$$

Then, equation (17) can be rewritten in the form of

$$\frac{f\,\mathrm{Re}}{64} = \frac{\dot{\gamma}_\mathrm{w}\eta_\mathrm{w}}{\dot{\gamma}_\mathrm{a}\eta_\mathrm{a}} = \phi\psi, \tag{18}$$

where the shear rate ratio ϕ and the viscosity ratio ψ are

$$\phi \equiv \frac{\dot{\gamma}_\mathrm{w}}{\dot{\gamma}_\mathrm{a}}, \tag{19}$$

$$\psi = \frac{\eta_\mathrm{w}}{\eta_\mathrm{a}}. \tag{20}$$

Note that $f\,\mathrm{Re}$ is the Poiseuille number. Since $\phi = \psi = 1$ for a Newtonian flow, the known Newtonian–Poiseuille number is obtained as

$$f_\mathrm{N}\,\mathrm{Re} = 64. \tag{21}$$

2.6 Power law models

For a power law fluid, which remains the most significant GNF model [16], the viscosity is described by the equation

$$\eta_\mathrm{p}(\dot{\gamma}) = K\dot{\gamma}^{n-1}, \tag{22}$$

where K is the consistency and n is the index. For power law fluids, the ratios by equations (19) and (20) are represented in the form of

$$\phi_\mathrm{p} = \frac{3n+1}{4n}, \tag{23}$$

$$\psi_\mathrm{p} = \phi_\mathrm{p}^{n-1}. \tag{24}$$

For $n = 1$, the Newtonian value is obtained as in equation (21).

2.7 Carreau model

The viscosity using the Carreau model is expressed as [10]

$$\eta(\dot{\gamma}) = \eta_\infty + (\eta_0 - \eta_\infty)(1 + \lambda^2\dot{\gamma}^2)^{\frac{n-1}{2}}, \tag{25}$$

where η_0 and η_∞ are the zero- and infinite-shear viscosities, respectively. Additionally, λ is the time constant. Substitution of equation (25) into equation (9) leads to [9,13]

$$I_1(\dot{\gamma}) = \frac{\pi R^3}{\lambda^4 \tau_w^3} \times \left[\begin{array}{c} G(\dot{\gamma};\eta_0, \eta_\infty, n, \lambda) \\ + \frac{\eta_\infty(\eta_0 - \eta_\infty)^2}{2n(n+1)}(1 + n(2n+1)\dot{\gamma}^4\lambda^4 \\ - (n-1)\dot{\gamma}^2\lambda^2)(1 + \dot{\gamma}^2\lambda^2)^{n-1} \\ + \frac{\eta_\infty^2(\eta_0 - \eta_\infty)}{(n+1)(n+3)}(2 + (n+2)(n+1)\dot{\gamma}^4\lambda^4 \\ - (n-1)\dot{\gamma}^2\lambda^2)(1 + \dot{\gamma}^2\lambda^2)^{\frac{n-1}{2}} \\ + \frac{\eta_\infty^3}{4}\dot{\gamma}^4\lambda^4 - \frac{(\eta_0 - \eta_\infty)^2\eta_\infty}{2n(n+1)} - \frac{2(\eta_0 - \eta_\infty)\eta_\infty^2}{(n+1)(n+3)} \end{array} \right], \quad (26)$$

where

$$G(\dot{\gamma};\ \eta_0, \eta_\infty, n, \lambda) = \begin{cases} \frac{(\eta_0 - \eta_\infty)^3}{(3n+1)(3n-1)}\left[(1 + \dot{\gamma}^2\lambda^2)^{\frac{3}{2}(n-1)} \right. \\ \left. \times \left(\begin{array}{c} \frac{2}{3} + n(3n-1)\dot{\gamma}^4\lambda^4 \\ -(n-1)\dot{\gamma}^2\lambda^2 \end{array} \right) - \frac{2}{3}\right] \text{for } n \neq \frac{1}{3} \\ \frac{(\eta_0 - \eta_\infty)^3}{6}\left[\frac{\lambda^2\dot{\gamma}^2(\lambda^2\dot{\gamma}^2 - 1)}{(1 + \lambda^2\dot{\gamma}^2)} + \ln(1 + \lambda^2\dot{\gamma}^2)\right] \\ \text{for } n = \frac{1}{3}. \end{cases} \quad (27)$$

Now, we are ready to calculate $\dot{\gamma}_w$ for a specified value Q by solving equation (11) ($Q = I_1(\dot{\gamma}_w)$). This will allow us to obtain an accurate value of ϕ. The nonlinearity in equation (26) is significant due to the presence of a logarithm and complex polynomials. Thus, it is essential to verify convergence with great care.

2.8 Viscosity ratio for the Carreau model

The Darcy friction factor in an actual case can be determined with the apparent shear rate by equation (18), which can be rewritten for the Carreau model as

$$\psi_c(\Gamma, \varphi, n, \phi) = \frac{\varphi + (1 - \varphi)(1 + \Gamma^2\phi^2)^{\frac{n-1}{2}}}{\varphi + (1 - \varphi)(1 + \Gamma^2)^{\frac{n-1}{2}}}, \quad (28)$$

where φ and Γ are defined as

$$\varphi = \frac{\eta_\infty}{\eta_0}, \quad (29)$$

$$\Gamma = \lambda\dot{\gamma}_a. \quad (30)$$

2.9 Expressions for correlations

The Carreau fluid renders a viscosity curve, as shown in Figure 2. As shown in the figure, the viscosity behaves like a Newtonian fluid in the low shear rate regime while it behaves like a power law one in the high shear regime. For the power law model, the following identity holds:

$$n - 1 \equiv \frac{\mathrm{d}\ln\eta_p}{\mathrm{d}\ln\dot{\gamma}} = \frac{\dot{\gamma}}{\eta_p}\frac{\mathrm{d}\eta_p}{\mathrm{d}\dot{\gamma}}. \quad (31)$$

It should be noted that both $\frac{\mathrm{d}\ln\eta_p}{\mathrm{d}\ln\dot{\gamma}}$ and ϕ_p are functions only of n, which is independent of K. Based on this idea, a method has been proposed to utilize this property even in more complex models. In this method, the original Carreau model can be approximated to a power law form by [1,7]

$$\eta(\dot{\gamma}) \approx K_1(\dot{\gamma}, \eta_\infty, \eta_0, \lambda, n)\dot{\gamma}^{n_1(\dot{\gamma},\eta_\infty,\eta_0,\lambda,n)-1}. \quad (32)$$

As mentioned, $K_1(\dot{\gamma}, \eta_\infty, \eta_0, \lambda, n)$ is not considered in the approximate evaluation of f, and $n_1(\dot{\gamma}_a, \eta_\infty, \eta_0, \lambda, n)$ is the only function of interest. Considering equation (31), the apparent index for a specific $\dot{\gamma}_a$ that characterizes the flow can be proposed as

$$n_1(\dot{\gamma}_a, \eta_\infty, \eta_0, \lambda, n) = \frac{\dot{\gamma}_a}{\eta(\dot{\gamma}_a)}\frac{\mathrm{d}\eta}{\mathrm{d}\dot{\gamma}}\bigg|_{\dot{\gamma}=\dot{\gamma}_a} + 1. \quad (33)$$

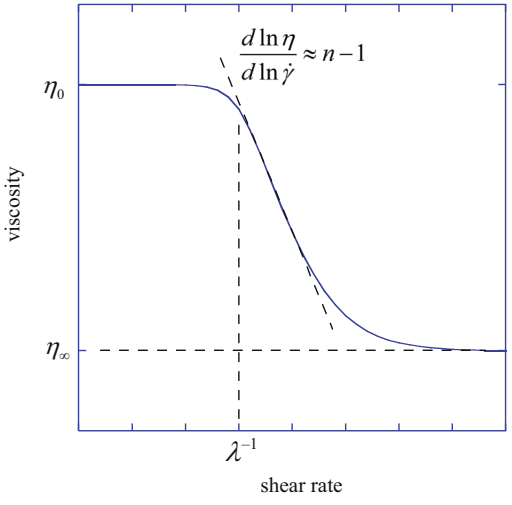

Figure 2: Carreau viscosity model with the shear rate.

For a Carreau fluid, the above relation can be rewritten as

$$n_1(\dot{\gamma}_a, \eta_\infty, \eta_0, \lambda, n) \equiv n_1(\Gamma, \varphi, n) = \left(1 - \frac{1}{1 + \left(\frac{1}{\varphi} - 1\right)(1 + \Gamma^2)^{\frac{n-1}{2}}}\right) \times \frac{(n-1)\Gamma^2}{(1 + \Gamma^2)^{\frac{n-1}{2}}} + 1. \quad (34)$$

Replacing the above quantity into equation (23), we obtain an approximate ϕ as

$$\phi_1 = \phi_p(n_1). \quad (35)$$

Since the velocity profiles by the power law and the Carreau model are different from each other, the core flow rates would be different, and thus, the friction factor. Thus, the mathematical foundation of the method seems weak and is thought to be a phenomenological methodology. Although this method yields an approximate friction factor in an efficient way, the bias from the accurate value is sometimes noticeable. To overcome this bias, this work modifies $n_1(\Gamma, \varphi, n)$ by introducing additional coefficients. The modified apparent index takes the form of

$$n_2(\Gamma, \varphi, n) = n_1\left(c\Gamma^d, \frac{\varphi}{h}, n\right), \quad (36)$$

where the coefficients c, d, and h represent real numbers that vary as functions of n. The modification of Γ stems from the fact that using the apparent shear rate is largely a matter of convention, lacking a strong physical foundation. Given that linear patterns are typically observed in logarithmic plots, the error can be adjusted using the term $C + d \ln \Gamma$. By setting C equal to the natural logarithm of c, we can replace Γ with $c\Gamma^d$ to enhance the overall accuracy of the model. Moreover, since the friction factor variation is known to change dramatically alongside φ, it is modified by a function as $\frac{\varphi}{h}$, where the functional form h will be discussed later. This adjustment aims to better align the theoretical framework with empirical observations, providing a more robust and precise representation of the underlying physical phenomena.

As a result, we have

$$n_2(\Gamma, \varphi, n) = \left(1 - \frac{1}{1 + \left(\frac{h}{\varphi} - 1\right)(1 + c^2\Gamma^{2d})^{\frac{n-1}{2}}}\right) \frac{(n-1)c^2\Gamma^{2d}}{(1 + c^2\Gamma^{2d})^{\frac{n-1}{2}}} + 1. \quad (37)$$

Then, n_2 becomes an input to equation (23) instead of n_1. Based on the solutions using equations (26) and (27), c, d, and h will provide an accurate correlation for the friction factor of the Carreau fluid. Then, ϕ is approximated by

$$\phi_2 = \phi_p(n_2). \quad (38)$$

The resulting Poiseuille number will be obtained by

$$f\,\mathrm{Re} = 64\phi_2\psi_c(\Gamma, \varphi, n, \phi_2). \quad (39)$$

When fully expanded, the above expression gives

$$f\,\mathrm{Re} = \left[48 + 16\left(\left(1 - \frac{1}{1 + \left(\frac{h}{\varphi} - 1\right)(1 + c^2\Gamma^{2d})^{\frac{n-1}{2}}}\right)\frac{(n-1)c^2\Gamma^{2d}}{(1 + c^2\Gamma^{2d})^{\frac{n-1}{2}}} + 1\right)^{-1}\right] \times \left[\frac{\varphi + (1-\varphi)(1 + \Gamma^2\phi^2)^{\frac{n-1}{2}}}{\varphi + (1-\varphi)(1 + \Gamma^2)^{\frac{n-1}{2}}}\right]. \quad (40)$$

2.10 Coefficient determination

Since the effects of $c(n)$ and $d(n)$ do not cause significant changes, linear functions are sufficient to describe their relationship as follows:

$$c(n) = c_0 + c_1 n, \quad (41)$$

$$d(n) = d_0 + d_1 n. \quad (42)$$

The variations related to $h(n)$, however, exhibit a high degree of complexity. To accurately capture these rapid fluctuations, an exponential function is required. Through trial and error, the following equation provides an appropriate representation for $h(n)$:

$$h(n) = h_0 - h_1 \exp(-h_2 n). \quad (43)$$

The determination procedure requires a regression with the exact data. For $f\,\mathrm{Re}$ by exact calculation and n_2 approximation to be equal, $\phi_2\psi_c(\Gamma, \varphi, n, \phi_2) = \phi\psi_c(\Gamma, \varphi, n, \phi)$ is required and is met by $\phi_2 = \phi$. To set an optimization problem, the following normalized shear rate ratio is introduced:

$$S(\Gamma_i, \varphi_j, n_k) = \frac{\phi(\Gamma_i, \varphi_j, n_k) - 1}{\phi_p - 1}. \quad (44)$$

Note that $\phi(\Gamma_i, \varphi_j, n_k)$ in the above expression is obtained by solving equation (11) using equation (26). In other words,

$$I_1(\dot{\gamma}_w) = Q \tag{45}$$

is solved by using $\phi = \dot{\gamma}_w/\dot{\gamma}_a$ (equation (19)). Likewise, ϕ_2 are normalized as

$$S_2(\Gamma_i, \varphi_j, n_k;\ \boldsymbol{c}) = \frac{\phi_2 - 1}{\phi_p - 1} = \frac{n_2(\Gamma_i, \varphi_j, n_k;\ \boldsymbol{c})^{-1} - 1}{n^{-1} - 1}. \tag{46}$$

Note that S_1 is expressed as

$$S_1(\Gamma_i, \varphi_j, n_k) = \frac{\phi_1 - 1}{\phi_p - 1} = \frac{n_1(\Gamma_i, \varphi_j, n_k)^{-1} - 1}{n^{-1} - 1}. \tag{47}$$

Then, the optimization problem is described as

$$\boldsymbol{c} = \arg\min_{\boldsymbol{c}} \sum_{i,j,k} [S(\Gamma_i, \varphi_j, n_k) - S_2(\Gamma_i, \varphi_j, n_k;\ \boldsymbol{c})]^2, \tag{48}$$

where $\boldsymbol{c} = [c_0, c_1, d_0, d_1, h_0, h_1, h_2]$.

Thus, the results for validation will be presented by comparing S and S_2. The optimization will be conducted using the generalized reduced gradient method.

3 Results

3.1 Shear rate ratio

As previously discussed, the wall shear rate is used to calculate the shear rate ratio, which in turn allows for the determination of the Poiseuille number. This shear rate ratio is a critical result, providing insights into friction characteristics based on the shear rate. Figure 3 illustrates how ϕ changes with respect to n and φ. Consistent with existing research, the variation in ϕ becomes limited as n increases. Additionally, higher φ values suppress changes in ϕ and reduce the influence of n.

As shown in Figure 3(a), when $\varphi = 0$, all four lines are parallel at large Γ values, the values of n decrease as Γ increases. When $\varphi = 0.001$, as shown in Figure 3(b), the value of ϕ decreases at large Γ. Additionally, when $n = 0.5$, the point where ϕ increases is delayed compared to when $n = 0.7$, causing the two curves to intersect. When $\varphi = 0.016$, the curve for $n = 0.5$ does not increase and remains below the curve for $n = 0.7$ across the entire high Γ range, as shown in Figure 3(c).

3.2 Normalization

Figure 3 shows a similarity in the patterns of change for the parameter φ for different values of n. To analyze this trend more effectively, Figure 4 presents the results after normalization. The graph displays results for 19 different n values, ranging from 0.05 to 0.95 in increments of 0.05. Each plot presents the results for φ starting from 0 and increasing 6.25×10^{-5} to 0.512 in doubling increments. For various engineering processes, ranging from low-velocity flows such as filtering to high-velocity flows like coating, the shear rate spans from 0.1 to 10^5 s^{-1}. In an extreme case where $\lambda = 10$ s and $n = 0$, the Γ range corresponds directly to the shear rate range. Therefore, the presented result encompasses all feasible processes involving Carreau fluids.

It is clear that for each n, the results change similarly with respect to φ. However, it is notable that as n increases, the point at which the decrease begins in relation to φ is delayed, as shown in Figure 4. A small value of n indicates that significant shear thinning is occurring. As n increases, there is a greater possibility that the viscosity and friction will be maintained while withstanding the influence of the solvent ($\varphi \neq 0$). It is important to remember that the

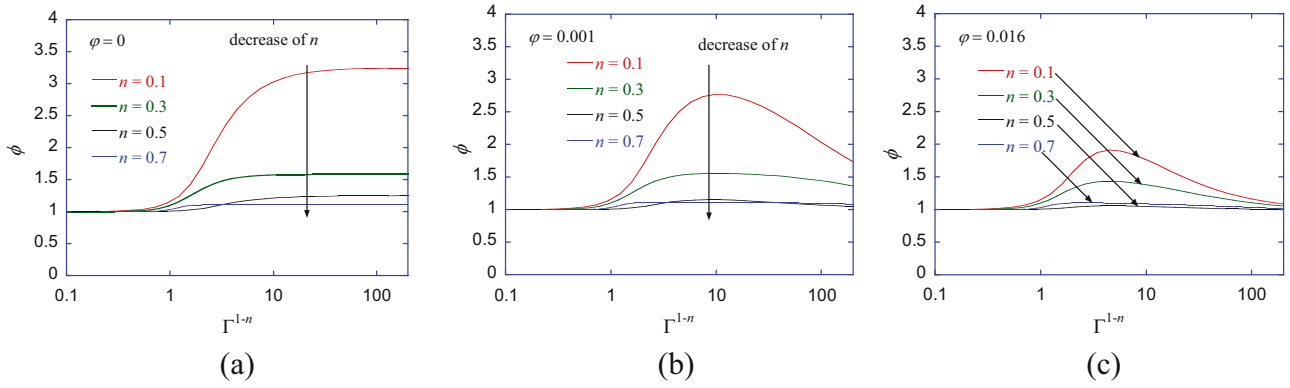

Figure 3: Shear rate ratio ϕ vs Γ^{1n} along with n = 0.1, 0.3, 0.5, and 0.7 for (a) $\varphi = 0$, (b) $\varphi = 0.001$, and (c) $\varphi = 0.016$.

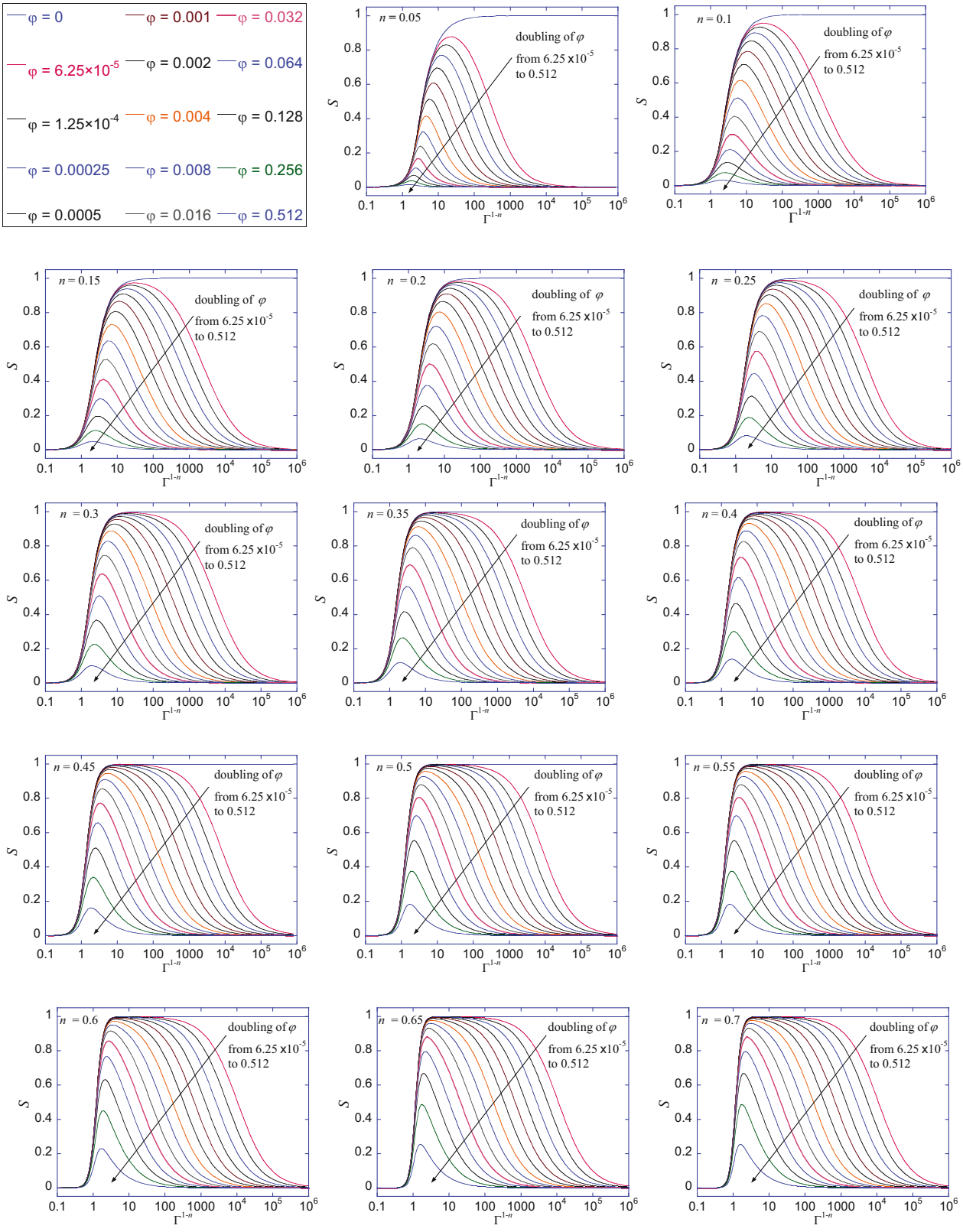

Figure 4: S vs Γ^{1n}, with φ shown concurrently. This is presented for all examined values of n, which range from 0.5 to 0.95 in increments of 0.05. Each specific n value is indicated within its respective figure. A legend in the top left corner of the graph provides information on the color scheme used for the φ curves.

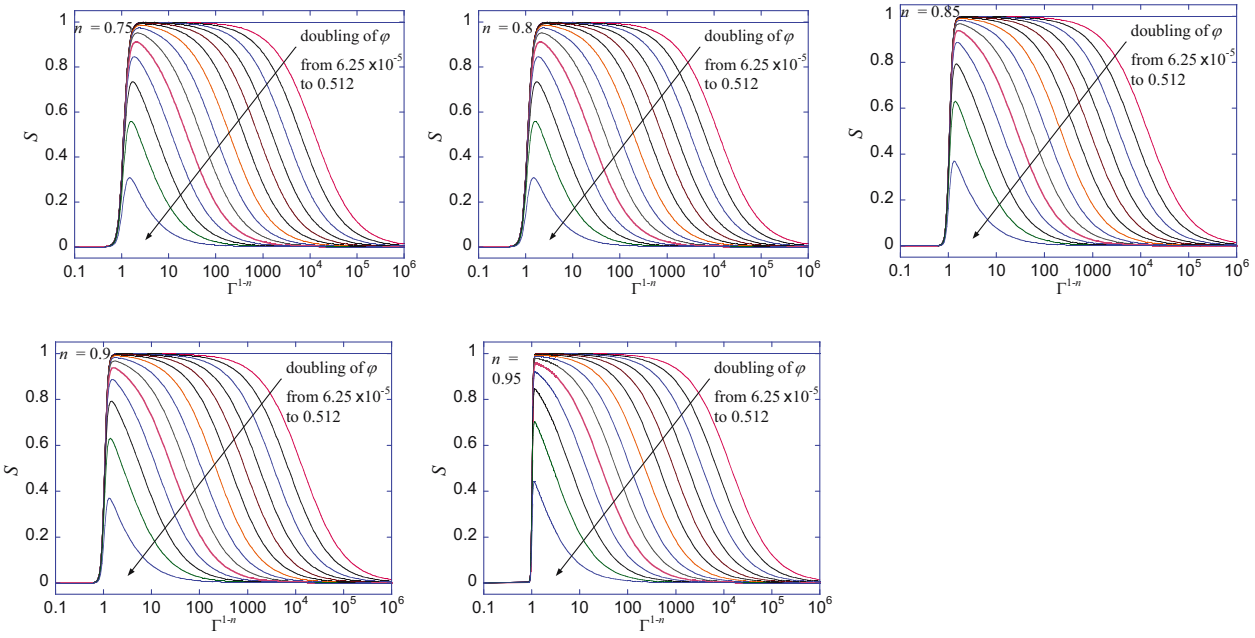

Figure 4: (*Continued*)

magnitude of n depends on structural changes such as alignment due to the shear rate. For a given n, the variation in φ yields interesting results. When φ is not equal to zero, the value of S increases from 0 to 1 as Γ increases and then returns to 0. Additionally, as φ increases, the change in S decreases, especially for larger values of Γ. This trend is observed in all 19 plots presented. As n increases, the increase in the curve near $\Gamma = 1$ becomes steeper, and the values gradually decrease to 0 for larger Γ. Consequently, larger values of n result in curves that are more asymmetric and skewed to the left. This result is shown in Figure 4 and will serve as base data for optimization.

Let us examine the case where n varies for the same φ. When $\varphi = 0$, S eventually asymptotes to 1 for large values of Γ, as shown in Figure 5(a). As n increases, the curve becomes steeper and approaches 1. However, for smaller n, the increase starts at lower values of Γ. As φ increases to 0.001, S decreases towards 0 as Γ increases. In Figure 5(b), the step-like curve transforms into a bell-shaped curve for small n, but as n increases, the curve shape approaches a step function followed by a gradual decay. When φ increases to 0.016, as shown in Figure 5(c), the overall decay becomes faster, and the peaks of the curves also decrease.

Despite the potential for minor inaccuracies in solving the nonlinear equation for wall shear rate, the propagation of errors through the friction factor and pressure drop calculations is not expected to be significantly amplified. The sensitivity of the friction factor to changes in the wall shear rate can be expressed as

$$\frac{\partial f}{\partial \dot{\gamma}} = \frac{64}{\mathrm{Re}}\left(\frac{\eta_w}{\dot{\gamma}_a \eta_a} + \frac{\dot{\gamma}_w}{\dot{\gamma}_a \eta_a}\frac{\partial \eta_w}{\partial \dot{\gamma}}\right), \tag{49}$$

where

$$\frac{\partial \eta_w}{\partial \dot{\gamma}} = (\eta_w - \eta_\infty)\frac{(n-1)\lambda^2 \dot{\gamma}_w^2}{1 + \lambda^2 \dot{\gamma}_w^2}. \tag{50}$$

Given that $\eta_w/\eta_a < 1$ and $|(n-1)\lambda^2\dot{\gamma}_w^2/(1+\lambda^2\dot{\gamma}_w^2)| < 1$, the error amplification is expected to be limited. This is further supported by the observation that $\lim_{\dot{\gamma}_w \to \infty} \partial f/\partial \dot{\gamma}_w = 0$, which is also confirmed through calculations. Consequently, the change in the friction factor can be approximated as $\Delta f \approx (\partial f/\partial \dot{\gamma}_w)\Delta \dot{\gamma}_w$, which is likely to be suppressed. As the pressure drop is calculated based on the friction factor, its variation would also be constrained. Therefore, any numerical errors arising from the solution of the nonlinear equation (equation (11)) are not expected to significantly impact the overall results.

3.3 Coefficient determination

The optimization process specified by equation (48) using data presented in Figure 4 was conducted. The optimization yielded a set of functions with specific coefficients, which are as follows:

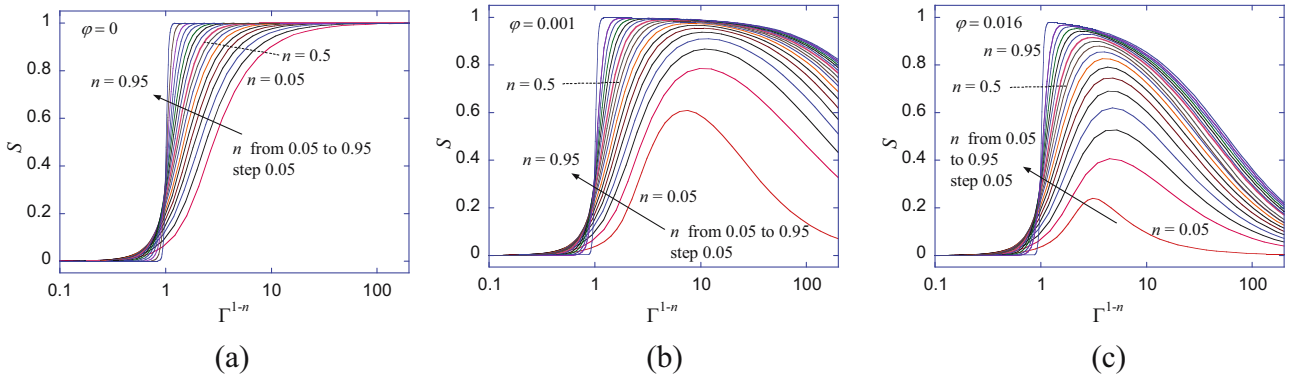

Figure 5: S vs Γ^{1n} alongside n with (a) $\varphi = 0$, (b) $\varphi = 0.001$, and (c) $\varphi = 0.016$. This is presented for all examined values of n, which range from 0.5 to 0.95 in increments of 0.05.

$$c(n) = 0.88669 - 0.14510n, \tag{51}$$

$$d(n) = 0.97899 + 0.030086n, \tag{52}$$

$$h(n) = 0.99828 - 0.37911\exp(-4.7989n). \tag{53}$$

Upon examination, it was observed that the function values exhibit close to unity, indicating that the optimized results do not significantly diverge from the initial n_1 approximation. This consistency suggests that the optimization procedure has refined the model while maintaining its fundamental characteristics.

Figure 6 illustrates the comparison of S values calculated using equations (19), (35), and (38). The results demonstrate that the values obtained from equation (35) do not deviate significantly from those derived using equation (19), suggesting limited room for improvement in this approach. However, the graph clearly shows that equation (38) yields noticeably improved results, indicating a more effective solution to the problem at hand. When calculating the overall correlation across the entire range, both cases yield a value of 0.999. However, in the shear rate range of 1–100 s^{-1}, the n_1 approximation results in a correlation of 0.985, while the n_2 approximation yields 0.999. The difference becomes more pronounced when examining maximum errors. As shown in Figure 6(a), when $\varphi = 0.001$, the maximum error decreases from 0.0783 to 0.0654, representing a 17% reduction; while, at $\varphi = 0.016$, the error significantly decreases from 0.0656 to 0.0263, reflecting a 60% reduction. As shown in Figure 6(b), when $\varphi = 0.001$, the error greatly decreases from 0.0852 to 0.0218, showing a 74% reduction, and at $\varphi = 0.016$, it also significantly decreases from 0.0807 to 0.0211, again a 74% reduction. As shown in Figure 6(c), the difference is even more substantial. When $\varphi = 0.001$, the error dramatically decreases from 0.104 to 0.018, an impressive 83% reduction; while, at $\varphi = 0.016$, it decreases from 0.0987 to 0.0155, resulting in an 84% reduction. These results demonstrate that the n_2 approximation generally leads to significant reductions in maximum errors across different conditions and figures.

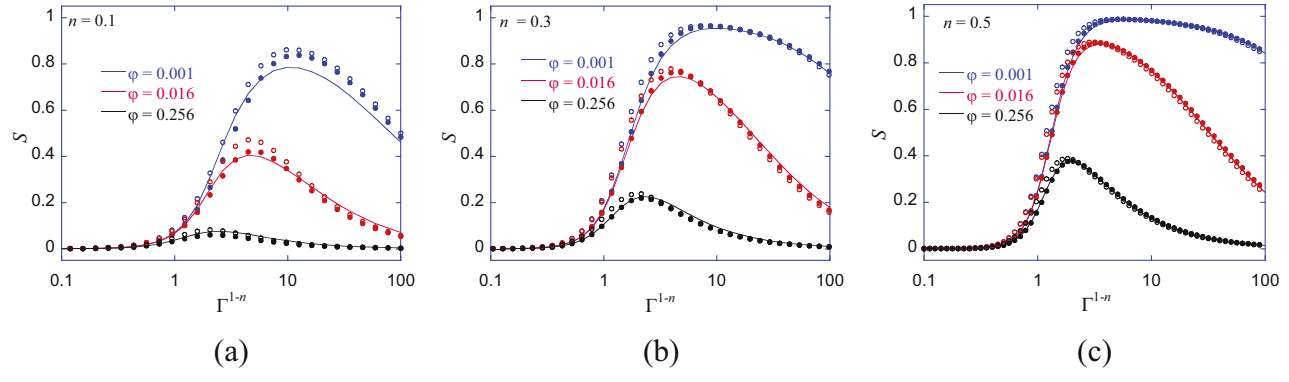

Figure 6: S vs Γ^{1n} with $\varphi = 0.001$, $\varphi = 0.016$, and $\varphi = 0.256$ in (a) $n = 0.1$, (b) $n = 0.3$ and (c) $n = 0.5$. Open circles show results from equation (47), filled circles show results from equation (46), and solid lines represent the results from equation (44).

3.4 Application

In this study, the PP melt, blood flow, and solvent-based coating paste were chosen as validation cases due to their representative nature as Carreau fluids. These non-Newtonian fluids exemplify shear-thinning behavior and hold significant importance in their respective fields: polymer processing for PP melt and the coating paste and biomedical applications for blood flow. These fluids offer rich experimental datasets and cover diverse ranges of viscosity and shear rates, allowing for comprehensive model validation across different conditions.

The Carreau model effectively describes the viscosity of PP melts. Studies have shown that PP melts exhibit a secondary Newtonian plateau at extremely high shear rates, typically between 10^6 and 10^7, which are impractical for most processing conditions. Therefore, it is reasonable to assume that $\varphi = 0$ for PP melts in practical applications. For a specific PP melt, the Carreau constants have been determined as follows: $\eta_0 = 936$ Pa s, $\eta_\infty = 0$ Pa s, $n = 0.4$, and $\lambda = 0.207$ s [17].

To illustrate the application of this model, consider the melt flow through a straight tube with a length of 1 m and a diameter of 10 mm, varying the flow rate from 10^{-8} to 0.001 m^3/s (0.01–1,000 cm^3/s). The analysis of this flow scenario yields insights into the relationship between the flow rate, friction factor, and pressure drop. As the flow rate increases from 0.01 to 1,000 cm^3/s, both f and Δp can be calculated, providing valuable information for processing considerations. It is important to note that this model does not account for shear heating, which could impact the results in real-world applications.

To account for shear heating effects, it is required to consider how viscosity changes with temperature rather than relying on an isothermal viscosity model. This consideration, however, falls outside the scope of the current study. The impact of shear heating is complex, depending on multiple fluid properties, including density, thermal conductivity, and heat capacity. As a result, it becomes challenging to validate the isothermal assumption by simply examining the total heat generation, which is typically calculated as the product of pressure drop and flow rate. A more comprehensive analysis would be required to accurately assess the significance of shear heating in the system [18]. Additionally, the Reynolds number should be verified to ensure that laminar flow conditions are maintained; in this particular case, the Re values remain well below the critical threshold for turbulent flow.

Figure 7(a) illustrates that the friction factor decreases as the flow rate increases, which is a characteristic phenomenon observed in shear-thinning fluids. As a result, the rate of pressure drop increase diminishes significantly after the inflection point of viscosity. This is associated with shear thinning, which is a result of chain alignment in polymer solutions or melts. When subjected to shear forces, the long, flexible polymer chains tend to orient themselves in the direction of flow. This alignment reduces the overall resistance to flow, leading to a decrease in

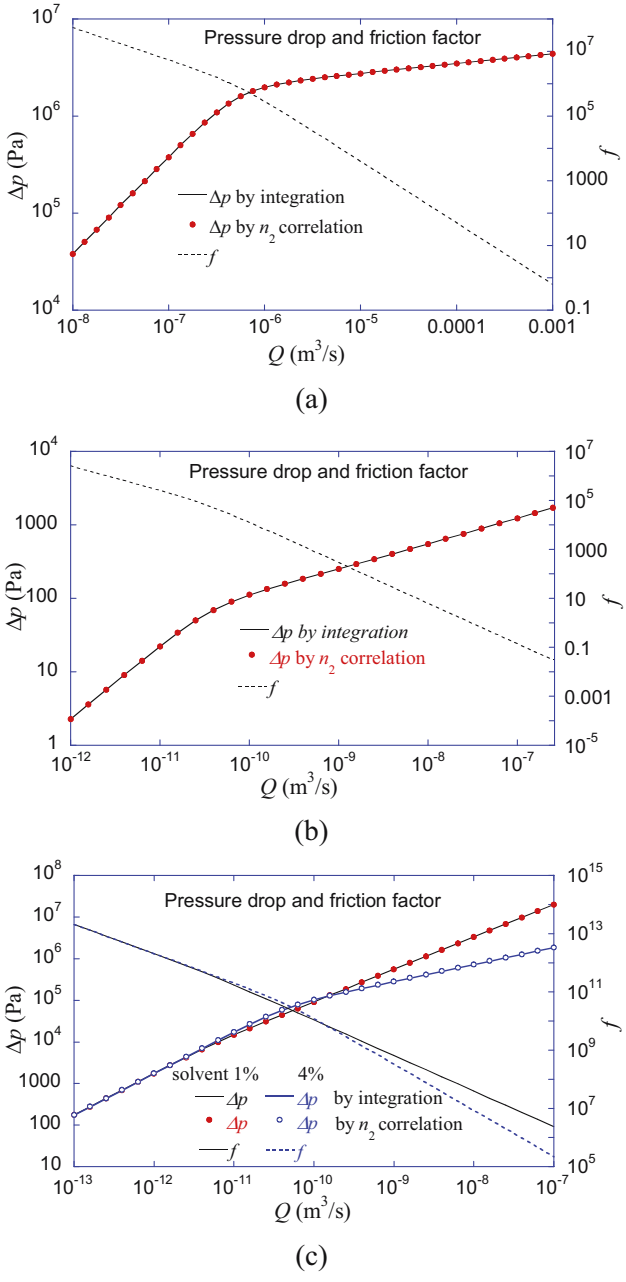

Figure 7: Pressure drop and friction factor plotted against the flow rate for (a) the PP melt [17], (b) blood [20], and (c) coating paste with solvent fractions of 1 and 4% [21]. The left vertical axis represents the pressure drop, while the right vertical axis represents friction.

viscosity as the shear rate increases [19]. Furthermore, we conducted a comparison between the pressure drop obtained through direct integration and that calculated using our proposed correlation. The figure demonstrates that these two sets of results are virtually indistinguishable, exhibiting an exceptionally close match. The root mean square error of the value obtained through correlation, compared to the value obtained through integration, is 0.023%. This high degree of agreement strongly supports the accuracy and validity of the developed correlation, effectively proving its reliability for practical applications. At a shear rate of 1,000/s, a 1% error in the wall shear rate results in errors of 1.6% in the friction factor and 0.96% in the pressure drop. In contrast, at a lower shear rate of 1 s^{-1}, the same 1% error leads to smaller errors: 0.97% in the friction factor and 0.43% in the pressure drop. These findings support the earlier assertion that the evaluation demonstrates low sensitivity to unexpected errors.

As a second case, a typical human blood, which shows the secondary Newtonian plateau, is considered ($\varphi \neq 0$). A representative dataset by the Carreau model is found in ref. [20]. The model constants are η_0 = 0.056 Pa s, η_∞ = 0.00345 Pa s, n = 0.3568, and λ = 3.313 s. In this scenario, we examine the blood flow through a tube with a length of 1 m and a diameter of 0.001 m. Figure 7(b) illustrates f and Δp as the flow rate varies from 10^{-12} to 2.6×10^{-7} m^3/s (0.000001–0.26 cm^3/s). The upper limit of the flow rate is set to maintain laminar flow conditions. As in the previous case, the friction factor exhibits a decreasing trend with increasing flow rate. The pressure drop values calculated through integration and those obtained from the correlation show close agreement. However, unlike the previous example, there is a slight discrepancy.

Upon closer inspection of Figure 7(b), one can observe that near the inflection point, the line representing the integrated values passes slightly below the center of the circular markers, indicating the correlation-derived values. This minor deviation is a manifestation of the error that occurs in Figure 6(b). Nevertheless, from an engineering perspective, this discrepancy is negligible and does not introduce significant errors that would impact the practical use of the correlation. The root mean square error of the value derived from correlation, relative to the value from integration, is 0.34%. The level of accuracy remains sufficient for engineering applications. Overall, the results demonstrate that the proposed method can accurately predict flow characteristics for Carreau fluids.

Additionally, let us consider the case of transporting paste used for fiber coating. It is known that viscosity changes significantly depending on the solvent fraction. According to the literature, when the solvent fraction is 1%, the viscosity parameters are η_0 = 11,000 Pa s, η_∞ = 0.1 Pa s, n = 0.78 and λ = 1,500 s. When the fraction increases to 4%, η_0 and η_∞ remains the same, but n decreases to 0.41 and λ to 170 s [21]. We aim to calculate the pressure drop when transporting this paste through a 4 mm diameter pipe at various flow rates.

Figure 7(c) shows that for 1% solvent, f decreases relatively linearly, while for 4% solvent, the index decreases and an inflection occurs in f due to shear thinning. As a result, at a flow rate of 10^{-7} m^3/s, the pressure drop for 4% solvent is more than 18 MPa lower than for 1% solvent. These calculation results prove invaluable for engineering applications, particularly in optimizing pump selection and designing efficient flow paths when provided with a specific viscosity model. The accuracy of the correlation-derived pressure drop values is noteworthy, with minimal deviations from the integration-based results. Specifically, the root mean square error is a mere 0.07% for the 1% solvent scenario and 0.13% for the 4% solvent case, demonstrating the high reliability of the correlation method in predicting pressure drops under varying solvent concentrations.

The application of this correlation is limited to the fully developed, isothermal single-phase laminar flow in straight tubes with uniform diameter, which guarantees a constant pressure gradient along the flow. It is important to note that the isothermal assumption may break down in cases of substantial shear heating, potentially resulting in viscosity reduction. Therefore, the current correlation cannot be directly applied to flows that involve transience, multiphase conditions, developments, curved geometry, compressibility [22], variable diameters, and turbulence. In addition, while it is highly unlikely that shear rates outside the range presented in this study will be considered, it should be noted that caution should be exercised when using the correlation in unusual situations where $n < 0.05$ or $\varphi > 0.512$, as this would constitute extrapolation beyond the validated range.

4 Conclusions

This work presents procedures for determining the Darcy friction factor for fully developed laminar flow of Carreau fluids in straight, circular tubes. In non-Newtonian flow, it has been demonstrated that the Darcy friction factor can be obtained using the ratio of the wall shear rate to the apparent shear rate. Therefore, it is necessary to accurately determine the wall shear rate under specific flow conditions.

For Carreau fluids, an equation was derived to calculate the wall shear rate for a given flow rate in a steady-state flow through circular tubes. This equation was solved iteratively for various flow rates to obtain baseline data for 19 different values of n, which were used to develop a correlation. By introducing a function that improves upon the existing method of simply using the apparent index, a new correlation was established. The correlation was found to be accurate for a wide range of shear rates. Its accuracy has been verified by applying it to the flow of the PP melt and blood flow.

The optimization technique developed in this study demonstrates significant potential for broader application across various viscosity models, offering a pathway to improve the accuracy of friction factor correlations for non-Newtonian fluids in general. By extending this method beyond Carreau fluids to encompass other models, such as Herschel–Bulkley or cross, researchers could establish more precise friction factor correlations applicable to a wider spectrum of non-Newtonian fluids. Furthermore, incorporating slip considerations into the correlation provides valuable insights for the design of flow systems, enhancing their efficiency and performance. This comprehensive approach not only advances our understanding of complex fluid behaviors but also offers practical tools for engineering applications involving non-Newtonian flows.

Funding information: This work was supported by NRF grants funded by the Korean government (NRF-2018R1A5A1024127 and 2020R1I1A2065650).

Author contribution: The author confirms the sole responsibility for the conception of the study, presented results and manuscript preparation.

Conflict of interest: The author declare no conflict of interest.

Ethical approval: The conducted research is not related to either human or animal use.

Data availability statement: All data generated or analyzed during this study are included in this published article.

References

[1] Skelland AHP. Non-Newtonian flow and heat transfer. New York: Wiley; 1966.
[2] Han C. Rheology and processing of polymeric materials: Volume 1: Polymer Rheology. Oxford: Oxford University Press; 2007.
[3] Kim SK, Kazmer DO, Colon AR, Coogan TJ, Peterson AM. Non-Newtonian modeling of contact pressure in fused filament fabrication. J Rheol. 2021;65(1):27–42.
[4] Capobianchi M, Wagner D. Heat transfer in laminar flows of extended modified power law fluids in rectangular ducts. Int J Heat Mass Transf. 2010;53:558–63.
[5] Hong J, Kim SK, Cho YH. Flow and solidification of semi-crystalline polymer during micro-injection molding. Int J Heat Mass Transf. 2020;153:119576.
[6] Kim SK, Kazmer DO. Non-isothermal non-Newtonian three-dimensional flow simulation of fused filament fabrication. Addit Manuf. 2022;55:102833.
[7] Cruz DA, Coelho PM, Alves MA. A simplified method for calculating heat transfer coefficients and friction factors in laminar pipe flow of non-Newtonian fluids. J Heat Transf. 2012;134(9):091703.
[8] Kim SK. Viscosity model based on Giesekus equation. Appl Rheol. 2024;34(1):20240004.
[9] Kim SK. Flow-rate based method for velocity of fully developed laminar flow in tubes. J Rheol. 2018;62:1397–407.
[10] Carreau PJ, Dekee D, Daroux M. Analysis of the viscous behavior of polymeric solutions. Can J Chem Eng. 1979;57:135–40.
[11] Kim SK. Collective viscosity model for shear thinning polymeric materials. Rheol Acta. 2020;59:63–72.
[12] Kumar M, Mondal PK. Leveraging perturbation method for the analysis of field-driven microflow of Carreau fluid. Microfluid Nanofluid. 2023;27:51.
[13] Kim SK. Darcy friction factor and Nusselt number in laminar tube flow of Carreau fluid. Rheol Acta. 2022;61(3):243–55.
[14] Sochi T. Analytical solutions for the flow of Carreau and Cross fluids in circular pipes and thin slits. Rheol Acta. 2015;54:745–56.
[15] Kim SK. Correlations for convective laminar heat transfer of Carreau fluid in straight tube flow. Energies. 2022;15(7):2368.
[16] Sarma R, Gaikwad H, Mondal PK. Effect of conjugate heat transfer on entropy generation in slip-driven microflow of power law fluids. Nanoscale Microsc Thermophys Eng. 2017;21(1):26–44.
[17] Thiébaud F, Gelin JC. Characterization of rheological behaviors of polypropylene/carbon nanotubes composites and modeling their flow in a twin-screw mixer. Compos Sci Technol. 2010;70(4):647–56.
[18] Ajeeb W, Oliveira MS, Martins N, Murshed SS. Performance evaluation of convective heat transfer and laminar flow of non-Newtonian MWCNTs in a circular tube. Therm Sci Eng Prog. 2021;25:101029.
[19] Parisi D, Han A, Seo J, Colby RH. Rheological response of entangled isotactic polypropylene melts in strong shear flows: Edge fracture, flow curves, and normal stresses. J Rheol. 2021;65(4):605–16.
[20] ITIS Foundation. Tissue properties [Internet]. Zurich: ITIS Foundation; 2021 [cited 2025 Feb 8]. https://itis.swiss/virtual-population/tissue-properties/database/.
[21] Zhao X, Stylios GK, Christie RM. Rheological behavior of polymer solutions during fabric coating. J Appl Polym Sci. 2008;107:2317–21.
[22] Kazmer DO, Colon AR, Peterson AM, Kim SK. Concurrent characterization of compressibility and viscosity in extrusion-based additive manufacturing of acrylonitrile butadiene styrene with fault diagnoses. Addit Manuf. 2021;46:102106.